

# Periodic Orbits and Gravitational Wave Radiation Mechanism in the Regular Hairy Black Hole

Liping Meng,<sup>1</sup> Zhaoyi Xu,<sup>1</sup> and Meirong Tang<sup>1,\*</sup>

<sup>1</sup>*College of Physics, Guizhou University,  
Guiyang 550025, China*

(Dated: November 5, 2024)

The extreme-mass-ratio inspiral (EMRI) system has extremely high research value in gravitational wave astronomy. Studying the evolution of their periodic orbits not only helps understand the nature of black holes but also reveals the long-term behavior of complex systems. In this paper, we derive the radial effective potential of a test particle and conduct an analysis of the marginally bound orbits (MBO) and the innermost stable circular orbits (ISCO). The results indicate that, as the hair parameter  $\beta$  increases, the associated parameters of MBO and ISCO decrease significantly. Based on these analyses, we explore the characteristics of periodic orbits in regular hairy black holes. The study reveals that, compared to the Schwarzschild black hole, the periodic orbits in regular hairy black holes correspond to lower energy, and test particles around them can maintain stability in orbits closer to the black hole. This finding provides a new perspective for distinguishing Schwarzschild black holes from hairy black holes and opens up new research avenues for testing the no-hair theorem. Finally, we analyze the gravitational waveforms of radiation from periodic orbits using the Kludge waveform method and find that variations in the hair parameter  $\beta$  introduce subtle modifications to the phase, period, and amplitude of the gravitational waves. These results not only aid in a better understanding of the dynamical properties of the regular hairy black hole but also provide insights for obtaining new clues about black hole properties through gravitational wave detection.

**Keywords:** Periodic orbits, EMRI system, Hairy black holes, Gravitational wave

## I. INTRODUCTION

General relativity provides a theoretical foundation for exploring the universe and has successfully predicted the existence of black holes[1–4]. The study of black hole physics originated from the pioneering work of J.R. Oppenheimer and H. Snyder[5]. Since then, black holes have become a focal point in the fields of general relativity and cosmology. The properties and behavior of black holes can be described through black hole solutions, which are a class of exact solutions derived from Einstein’s field equations under specific conditions. The classical black hole solutions include the Schwarzschild solution[6, 7], the Kerr solution[8, 9], the Reissner-Nordström (RN) solution[10–12], and the Kerr-Newman solution[13, 14]. In the above black hole solutions, black holes are completely described solely by their mass  $M$ , angular momentum  $J$ , and charge  $Q$ , adhering to the no-hair theorem[15, 16]. However, the appearance of the BBMB black hole challenged the no-hair theorem. First proposed by Bocharova, Bronnikov, Melnikov, and Bekenstein[17], it was the first exact black hole solution found to include a scalar field and represents a black hole only in four-dimensional space[18]. Subsequently, within the framework of Einstein-Yang-Mills theory, Piotr Bizon was the first to obtain a “colored” black hole solution using numerical methods[19]. These discoveries have encouraged researchers to explore more hairy black hole

solutions (see references such as [20–23]). The emergence of hairy black holes challenges the traditional information paradox[24], providing important clues for understanding the formation and evolution of black holes. Therefore, further research on hairy black holes will help characterize the physical properties of black holes more precisely and deepen our understanding of black hole behavior. These studies will further clarify the role of black holes in cosmic structure and astrophysical evolution, providing a more reliable scientific foundation for the development of astrophysics and black hole theory.

Meanwhile, the extreme-mass-ratio inspiral (EMRI) system is also an important field for studying black hole properties[25]. This system consists of a stellar-mass compact object (such as a neutron star, white dwarf, or black hole) and a supermassive black hole[26], with a typical mass ratio of  $10^{-4}$  to  $10^{-7}$ . With the successful detection of gravitational waves from binary black hole mergers[27, 28], the era of gravitational wave astronomy has officially begun. This breakthrough not only advances research on black holes and their merger mechanisms but also makes the EMRI system particularly important in astronomy and gravitational wave studies, as the EMRI system is considered one of the key signal sources in gravitational wave observations[25, 29]. Additionally, the EMRI system holds research value in other areas, such as testing for the presence of dark matter around massive black holes[30–32], constraining cosmological parameters[33], and verifying general relativity[34].

It is well known that periodic orbits exist around black holes[35–37]. Moreover, in the EMRI system, periodic or-

---

\* Electronic address: tangmr@gzu.edu.cn (Corresponding author)

bits can radiate gravitational waves[35, 38]. By observing these gravitational wave waveforms, more information can be obtained about the orbital dynamical characteristics of stellar-mass celestial bodies and the formation of supermassive black holes and the basic mechanisms of the universe[29]. This prompts us to conduct a preliminary exploration of the periodic orbits of a timelike test particle around a regular hairy black hole and the gravitational waves radiated by the EMRI system. It is worth noting that bound orbits around black holes are divided into two types. One type is the precessing orbit, whose study began with one of the key cases in testing general relativity: the precession of Mercury's perihelion[39]. Subsequently, research on the precessing orbits of stars around Sgr A\* has also received extensive attention and in-depth discussion[40, 41]. These investigations have found valuable applications in constraining theories of gravity[42, 43]. The other type of orbit is the periodic orbit, which plays an important role in the study of gravitational wave radiation[38]. It is widely believed that periodic orbits can provide more information about the fundamental nature of black holes. Therefore, research on periodic orbits is of great significance for understanding the formation mechanisms of black holes and the properties of particle trajectories around them.

In light of this, Janna Levin and others proposed a classification method for periodic orbits[35]. Each orbit is represented by three integers  $z$ ,  $w$ , and  $v$ , which respectively denote the scaling, rotation, and vertex behavior of the orbit, thereby defining the quantity  $q = \frac{w+v}{z}$ . When  $q$  is an irrational number, the orbit is a precessing orbit, where each subsequent orbit undergoes a precession relative to the previous one[44, 45]. When  $q$  is a rational number, the orbit is periodic, and a particle undergoing periodic orbital motion will, after a finite number of repetitions, return precisely to its initial state. Notably, the precessing orbit of a particle can be seen as a perturbation of a periodic orbit[35]. Therefore, studying periodic orbits can reveal properties related to precessing orbits and provide physical insights into black holes. Currently, this classification method has been extensively studied in various types of black holes, including Kerr black holes[46–48], Schwarzschild black holes[49], Einstein-Lovelock black holes[50], binary black hole systems[51], charged black holes[52], spherically symmetric naked singularities[53], and polymer black holes[54].

Finally, studying hairy black holes is of great significance for understanding the properties and physical characteristics of black holes. The proposal of the hairy black hole model breaks the standard no-hair theorem, allowing black holes to have more characteristic parameters[55, 56]. Therefore, hairy black holes can provide more physical information about black holes. In this case, the study of periodic orbits is particularly important because they can more sensitively capture the physical effects brought by these additional hairy parameters[57, 58]. In particular, in EMRI systems,

timelike test particles moving along the periodic orbits of hairy black holes will exhibit unique signal characteristics in gravitational wave radiation, which has important observational significance for the verification and expansion of the no-hair theorem. In addition, the EMRI system itself is one of the important targets of future gravitational wave detection missions (such as the Laser Interferometer Space Antenna[59], Taiji[60], and TianQin[61]). The gravitational wave signals generated by the system help finely detect the spacetime structure around black holes, thus distinguishing a regular hairy black hole from the traditional Schwarzschild or Kerr black hole. Therefore, studying the periodic orbits and gravitational wave characteristics in the context of hairy black holes can not only deepen our understanding of black holes but also provide a rich theoretical support and data interpretation framework for future gravitational wave observations.

In this paper, we mainly discuss the periodic orbits of a timelike test particle in the background of a regular hairy black hole and preliminarily study the characteristics of gravitational waves generated by periodic orbits in the EMRI system in this background. The structure of this paper is as follows: In Section 2, we give a brief introduction to the regular hairy black hole and calculate the effective potential of a timelike test particle around it. In Section 3, in the first subsection, we introduce the relevant properties of MBO and ISCO; in the second subsection, we introduce periodic orbits. In Section 4, we conduct a preliminary exploration of the gravitational waves radiated by periodic orbits. Finally, in Section 5, a summary is given. In this paper, unless otherwise specified, the natural unit system with  $c = G = 1$  is used throughout.

## II. THE REGULAR HAIRY BLACK HOLE

Wheeler and others proposed the no-hair theorem for black holes. That is, within the framework of general relativity, all the properties of a black hole are determined only by the mass  $M$ , angular momentum  $J$ , and electric charge  $Q$  of the black hole[15, 16]. However, in one case, when there are various nonlinear matter fields outside the black hole, the no-hair theorem will no longer apply[62, 63]. In another case, under the Einstein-Yang-Mills theory, black holes can exhibit additional hairs[64, 65]. Among them, Piotr Bizon was the first to analyze the static spherically symmetric Einstein-Yang-Mills equation with the  $SU(2)$  gauge group and obtained a “colored” black hole solution through numerical methods[19]. This discovery has promoted researchers' exploration of more hairy black hole solutions. For example, hairy black hole solutions in multi-dimensional spacetimes[21, 22, 66, 67] and some hairy black hole solutions constructed by scholars using the method of gravitational decoupling[20, 23, 68–70]. In this paper, we briefly review the black hole solution obtained by scholars such as Jorge Ovalle through the gravitational decou-

pling analysis method. Its metric form is

$$ds^2 = -e^{\nu(r)} dt^2 + e^{\lambda(r)} dr^2 + r^2 d\Omega^2, \quad (1)$$

$$e^{\nu} = e^{-\lambda} = 1 - \frac{2M}{r} + \frac{e^{-\alpha r/M}}{rM} (\alpha^2 r^2 + 2M\alpha r + 2M^2). \quad (2)$$

Where  $\nu = \nu(r)$ ,  $\lambda = \lambda(r)$  are functions of  $r$ , and  $d\Omega^2 = d\theta^2 + \sin^2\theta d\phi^2$ .  $M$  is the black hole mass, and  $\alpha$  is the hairy parameter. In addition, due to the introduction of the tensor vacuum, a matter source that causes the deformation of the Minkowski vacuum in [23], the singularity of the seed metric (Schwarzschild metric) at  $r = 0$  is eliminated. Therefore, the metric described above is a regular hairy black hole.

For the convenience of later calculations, here we let  $\beta = \frac{1}{\alpha}$ . The metric (1) is rewritten as

$$ds^2 = -f(r)dt^2 + f(r)^{-1}dr^2 + r^2d\theta^2 + r^2\sin^2\theta d\phi^2, \quad (3)$$

$$\begin{aligned} ds^2 = & -\left[1 - \frac{2M}{r} + \frac{e^{-r/\beta M}}{rM} \left(\frac{r^2}{\beta^2} + \frac{2Mr}{\beta} + 2M^2\right)\right] dt^2 \\ & + \left[1 - \frac{2M}{r} + \frac{e^{-r/\beta M}}{rM} \left(\frac{r^2}{\beta^2} + \frac{2Mr}{\beta} + 2M^2\right)\right]^{-1} dr^2 \\ & + r^2 d\theta^2 + r^2 \sin^2\theta d\phi^2. \end{aligned} \quad (4)$$

Analyzing the above equation, when  $\beta \rightarrow 0$ , the black hole solution reverts to the Schwarzschild solution; when  $\beta \rightarrow \infty$ , the Minkowski spacetime is obtained. Combined with Figure 1, the event horizon information of a regular hairy black hole ( $f(r) = 0$ ) can be obtained. Obviously, when  $\beta < 0.3906$ , there is a black hole with two event horizons; when  $\beta_0 = 0.3906$ , there is an extremal black hole with only one event horizon (orange solid line); when  $\beta > 0.3906$ , there is a spacetime without a black hole. When  $\beta \rightarrow \infty$ , this corresponds to an asymptotically flat spacetime, which is represented by the red solid line in the figure. In addition, the event horizon radius of the Schwarzschild black hole is significantly smaller than the event horizon radius of the regular hairy black hole (the black solid line in the figure represents the event horizon of the Schwarzschild black hole).

For the timelike geodesics in the EMRI system, considering the motion of a test particle with stellar mass around a regular hairy black hole, on the equatorial plane ( $\theta = \frac{\pi}{2}, \dot{\theta} = 0$ ), the Lagrangian of the test particle is

$$\mathcal{L} = \frac{1}{2} m g_{\mu\nu} \dot{x}^\mu \dot{x}^\nu = \frac{1}{2} m (-e^{\nu(r)} \dot{t}^2 + e^{\lambda(r)} \dot{r}^2 + r^2 \dot{\phi}^2). \quad (5)$$

Among them, the “.” here represents the derivative with respect to proper time  $\tau$ .  $m$  represents the mass of the test particle, and in the subsequent discussion, it is set that  $m = 1$ . The generalized momentum of the test particle is defined by the following equation.

$$P_\mu = \frac{\partial \mathcal{L}}{\partial \dot{x}^\mu} = g_{\mu\nu} \dot{x}^\nu. \quad (6)$$

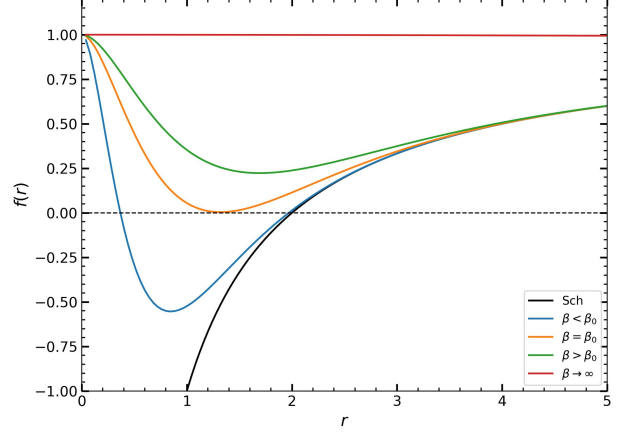


FIG. 1: The event horizon information of a regular hairy black hole. Here, the parameter  $\beta_0 = 0.3906$  represents an extremal black hole. Where  $M = 1$ .

According to the above equation, the four equations of motion of the particle can be obtained as

$$P_t = -\left[1 - \frac{2M}{r} + \frac{e^{-r/\beta M}}{rM} \left(\frac{r^2}{\beta^2} + \frac{2Mr}{\beta} + 2M^2\right)\right] \dot{t} = -E, \quad (7)$$

$$P_r = \left[1 - \frac{2M}{r} + \frac{e^{-r/\beta M}}{rM} \left(\frac{r^2}{\beta^2} + \frac{2Mr}{\beta} + 2M^2\right)\right]^{-1} \dot{r}, \quad (8)$$

$$P_\theta = r^2 \dot{\theta} = 0, \quad (9)$$

$$P_\phi = r^2 \dot{\phi} = L. \quad (10)$$

In the above equation,  $E$  represents the energy per unit mass of the particle, and  $L$  represents the orbital angular momentum per unit mass of the particle. From equations (7) and (10), it can be found that

$$\dot{t} = \frac{E}{\left[1 - \frac{2M}{r} + \frac{e^{-r/\beta M}}{rM} \left(\frac{r^2}{\beta^2} + \frac{2Mr}{\beta} + 2M^2\right)\right]}, \quad (11)$$

$$\dot{\phi} = \frac{L}{r^2}. \quad (12)$$

For a massive test particle, its four-dimensional velocity is a timelike unit vector. Therefore, there exists  $g_{\mu\nu} \dot{x}^\mu \dot{x}^\nu = -1$ . Substituting equations (11) and (12) into equation (5) can simplify the Lagrangian to

$$\begin{aligned} & \frac{\dot{r}^2}{\left[1 - \frac{2M}{r} + \frac{e^{-r/\beta M}}{rM} \left(\frac{r^2}{\beta^2} + \frac{2Mr}{\beta} + 2M^2\right)\right]} + \frac{L^2}{r^2} \\ & - \frac{E^2}{\left[1 - \frac{2M}{r} + \frac{e^{-r/\beta M}}{rM} \left(\frac{r^2}{\beta^2} + \frac{2Mr}{\beta} + 2M^2\right)\right]} = -1. \end{aligned} \quad (13)$$

Rewrite the above equation as

$$\dot{r}^2 = E^2 - V_{eff}, \quad (14)$$

here

$$V_{eff} = \left[1 - \frac{2M}{r} + \frac{e^{-r/\beta M}}{rM} \left(\frac{r^2}{\beta^2} + \frac{2Mr}{\beta} + 2M^2\right)\right] \left(1 + \frac{L^2}{r^2}\right). \quad (15)$$

The above equation is the effective potential for the radial motion of the particle. We will conduct a detailed analysis of the properties of the effective potential in Figure 2. From the first figure in Figure 2, it can be obtained that as the orbital angular momentum decreases, the two extreme values of the effective potential gradually approach each other and finally converge at one point. This line corresponds to the innermost stable circular orbit (ISCO) of the particle's motion, that is, the blue solid line shown when  $L = 3.464$ . The maximum value of the effective potential corresponds to the marginally bound orbit (MBO) of the particle, that is, the purple solid line shown when  $L = 3.996$ . At this time,  $V_{eff} = E = 1$ . These two kinds of orbits will be introduced in detail in the next section. From the second figure in Figure 2, it can be obtained that as the hairy parameter increases, the extreme value of the effective potential gradually increases. Here, when the hairy parameter is equal to zero, it corresponds to the Schwarzschild black hole case. In addition, by combining equations (14) and (15), we find that when  $r \rightarrow \infty$ ,  $V = 1$ . Therefore, when  $E \geq 1$ , there is no bound orbit and the particle can move to infinity; when  $E < 1$ , there is a bound orbit for the motion of the test particle. The specific situation will be shown in the next section.

### III. THE MARGINALLY BOUND ORBIT (MBO), THE INNERMOST STABLE CIRCULAR ORBIT (ISCO), AND PERIODIC ORBITS

In a strong gravitational field, particles around black holes will exhibit complex trajectories. Studying the properties of the trajectories of particles around black holes can indirectly obtain physical information about black holes. In this section, we mainly study three types of orbits of test particles: the marginally bound orbit (MBO), the innermost stable circular orbit (ISCO), and periodic orbits.

#### A. Relevant properties of MBO and ISCO

The particle is in a marginally bound state on the MBO. A particle on this orbit has the same energy as a stationary particle at infinity, and a small additional perturbation on the particle will cause it to escape from the gravitational field of the black hole to infinity or spiral into the black hole. This marginally bound orbit is defined by the following conditions.

$$V_{eff} = E = 1, \quad \partial_r V_{eff} = 0. \quad (16)$$

Numerical solution of equations above can draw the relationship diagrams of MBO radius and hairy parameter  $\beta$ , as well as  $L_{MBO}$  and hairy parameter  $\beta$ , as shown in Figure 3. It is obvious from Figure 3 that as the hairy parameter  $\beta$  increases, both  $r_{MBO}$  and  $L_{MBO}$  show a decreasing trend. In the initial stage, as the hairy parameter  $\beta$  changes, the change trends of  $r_{MBO}$  and  $L_{MBO}$  are not obvious. This indicates that at this time, the difference between a regular hairy black hole and a Schwarzschild black hole is very small and not easy to distinguish. When the hairy parameter is close to the critical value  $\beta_0$  of an extremal black hole, the difference between the corresponding orbital parameters and the Schwarzschild black hole is significantly enhanced. Therefore, fine measurements of orbital behavior near  $\beta_0$  may provide strong observational evidence and theoretical support for further verification of the no-hair theorem.

The ISCO is the orbit with the smallest radius at which a particle can maintain stable circular motion near a black hole. However, if the particle's energy is less than the energy of the particle on the ISCO, that is,  $E < E_{ISCO}$ , it will be unstable and cause the particle to spiral into the black hole. The ISCO is defined as

$$\dot{r} = 0, \quad \partial_r V_{eff} = 0, \quad \partial_r^2 V_{eff} = 0. \quad (17)$$

Numerical solution of equations above can draw the variation of ISCO radius  $r_{ISCO}$ , angular momentum  $L_{ISCO}$ , and energy  $E_{ISCO}$  with the hairy parameter  $\beta$ . As shown in Figure 4, with the increase of the hairy parameter  $\beta$ , the radius  $r_{ISCO}$ , angular momentum  $L_{ISCO}$ , and energy  $E_{ISCO}$  of the ISCO all show a slow decreasing trend in the initial stage. Compared with the corresponding values of the Schwarzschild black hole, these changes are not significant. (In the figure, when the hairy parameter  $\beta = 0$ , the regular hairy black hole degenerates into a Schwarzschild black hole. At this time,  $r_{ISCO} = 6$ , which is consistent with the calculation result of the Schwarzschild black hole[71, 72].) However, when the parameter  $\beta$  approaches the case of an extremal black hole, the changes in  $r_{ISCO}$ ,  $L_{ISCO}$ , and  $E_{ISCO}$  decrease significantly. That is, when the hairy parameter is close to the critical value  $\beta_0$  corresponding to an extremal black hole, the differences between these orbital parameters and the Schwarzschild black hole are significantly enhanced. Therefore, measurements near  $\beta_0$  (such as periodic orbits) are expected to further test the no-hair theorem by distinguishing the regular hairy black hole from a Schwarzschild black hole.

In addition, according to the previous analysis, we find that there should be an allowed region for the orbital angular momentum and energy of the particle that satisfy the bound orbit motion. As shown in Figure 5, when  $\beta = 0.25$  and  $L = 0.5(L_{MBO} + L_{ISCO})$ , the energy  $E$  of the bound orbit is in the range of (0.9546, 0.9684). Secondly, it can also be obtained from Figure 5 that when the two extreme values of the  $\dot{r}^2 - r$  curve are of opposite signs, the orbit represented at this time is a bound orbit. Further, the  $(L, E)$  region of the bound orbit can

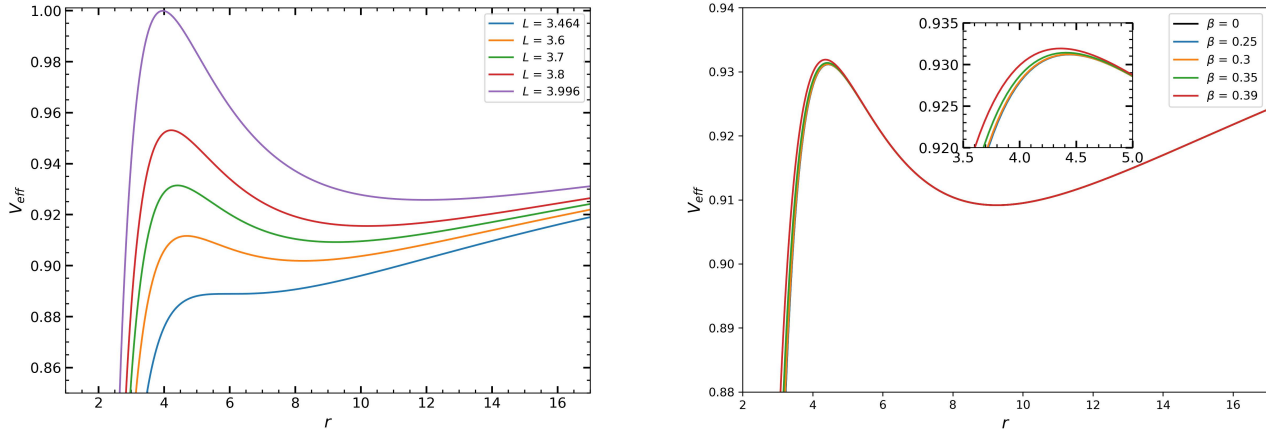


FIG. 2: The relationship diagram between the effective potential  $V_{eff}$  and the radial radius  $r$ . Here,  $M = 1$ . In the first figure, fix  $\beta = 0.35$ . From the blue solid line to the purple solid line,  $L$  is 3.464, 3.6, 3.7, 3.8, and 3.996 in turn. In the second figure, fix  $L = 3.7$ . From bottom to top, the solid lines of  $\beta$  values are 0, 0.25, 0.3, 0.35, and 0.39 in turn.

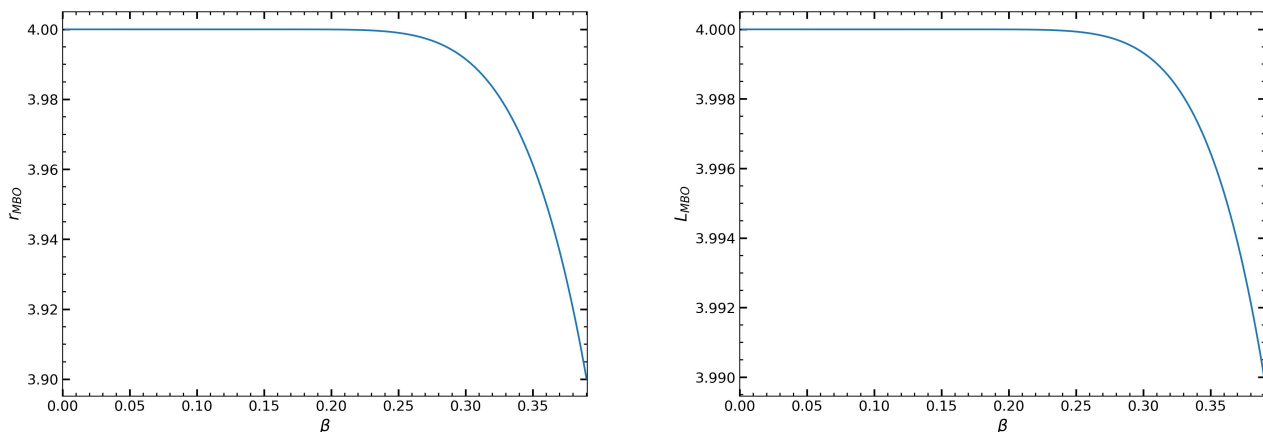


FIG. 3: The properties of the MBO of the particle around a regular hairy black hole. Take  $M = 1$ . The first figure is the  $r_{MBO} - \beta$  relationship diagram; the second figure is the  $L_{MBO} - \beta$  relationship diagram. Here  $\beta$  is the hairy parameter.

be obtained, as shown by the shaded area in Figure 6. In Figure 6, we have plotted the  $(L, E)$  parameter space for  $\beta = 0$  and  $\beta = 0.39$ . Obviously, as the parameter  $\beta$  increases, the parameter space has a tendency to decrease and the allowed energy range of the bound orbit of the test particle increases. The uppermost and lowermost boundary points of the parameter space are  $E_{MBO}$  and  $E_{ISCO}$  corresponding to different orbital angular momenta respectively.

## B. Periodic orbits

Periodic orbits are an effective method for studying the dynamics of test particles around black holes. Before studying periodic orbits, we need to understand quasi-periodic orbits, that is, precessional orbits also known as general orbits. A general orbit refers to an orbit where a particle does not exactly return to its initial state after repeated motions. Its next orbit will have a precession from the previous orbit[73]. In this case, the corresponding  $q$  (as shown in formula (18)) will be an irrational number. Since the general orbit of particle motion around a black hole can be regarded as a perturbation of a peri-

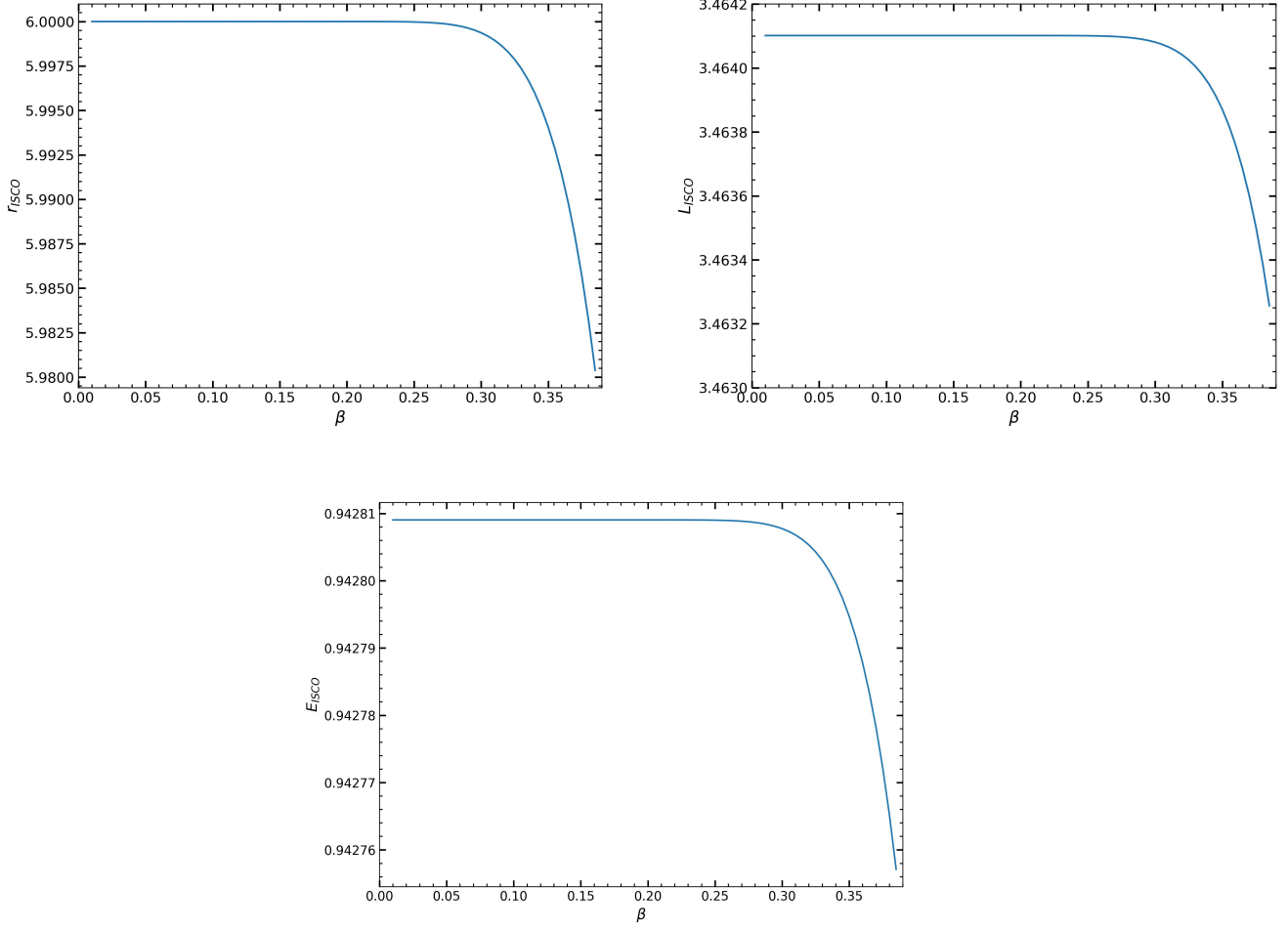


FIG. 4: The properties of the ISCO of the particle around a regular hairy black hole. Take  $M = 1$ . The first figure is the  $r_{ISCO} - \beta$  relationship diagram; the second figure is the  $L_{ISCO} - \beta$  relationship diagram; the third figure is the  $E_{ISCO} - \beta$  relationship diagram.

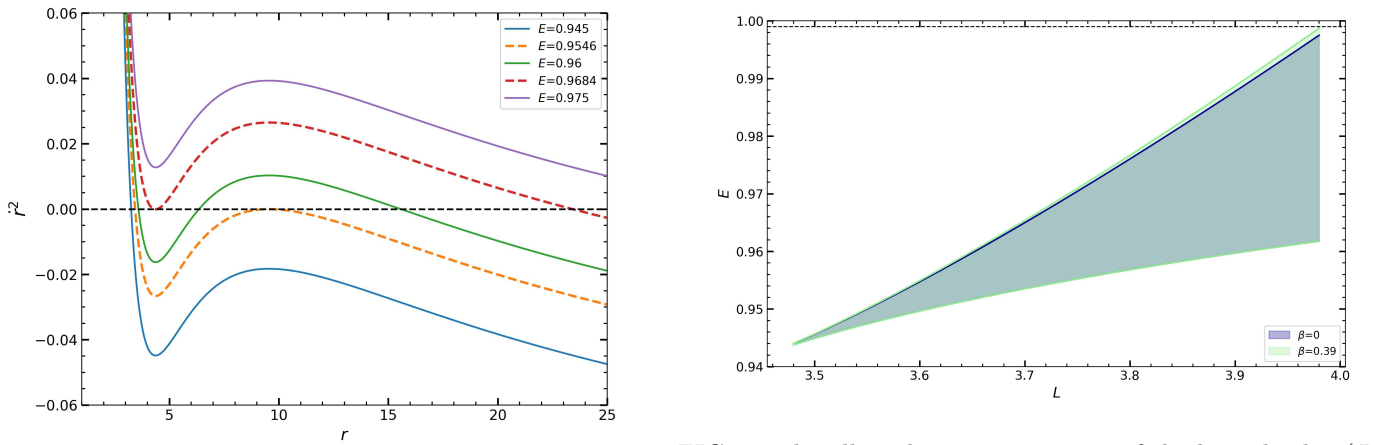


FIG. 5: The relationship diagram of  $\dot{r}^2 - r$ . Here, take  $M = 1$ ,  $\beta = 0.25$ , and  $L = 0.5(L_{MBO} + L_{ISCO})$ .

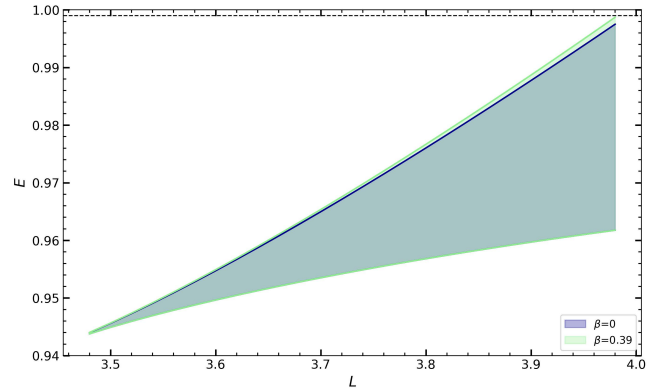


FIG. 6: The allowed parameter space of the bound orbit  $(L, E)$  of the test particle around the regular hairy black hole. Here,  $M = 1$ .

odic orbit[35]. Therefore, studying periodic orbits is of great significance for understanding the properties of the orbits of particles around black holes.

A periodic orbit refers to an orbit where a test particle can return to its initial state within a finite time. It is a bound orbit. According to the classification method of particle periodic orbits proposed in the literature[35], use three integers  $(z, w, v)$  to define a rational number  $q$ , and establish the relationship between it and a definite periodic orbit. Here,  $q$  is defined by the following

$$q = \frac{1}{\pi} \int_{r_1}^{r_2} \frac{\dot{\phi}}{\dot{r}} dr - 1 = \frac{1}{\pi} \int_{r_1}^{r_2} \frac{L}{r^2 \sqrt{E^2 - [1 - \frac{2M}{r} + \frac{e^{-r/\beta M}}{rM} (\frac{r^2}{\beta^2} + \frac{2Mr}{\beta} + 2M^2)] (1 + \frac{L^2}{r^2})}} dr - 1. \quad (20)$$

Here,  $r_1$  and  $r_2$  are the periapsis radius and the apoapsis radius.

As known from Figure 6, there is an allowed parameter space for energy  $E$  and orbital angular momentum  $L$ . Therefore, according to equation (20), by fixing one of  $E$  or  $L$  and the parameter  $\beta$ , the relationship diagram of  $q$  and  $E$  or  $L$  can be drawn. As shown in Figure 7. From figures (a) and (b) of Figure 7, it can be obtained that different orbital angular momenta correspond to different energy value ranges, which is in line with the situation shown in Figure 6. From the  $q - E$  relationship diagram, it can also be analyzed that as the energy  $E$  increases,  $q$  increases slowly. When the energy  $E$  is in the extreme value situation, the rational number  $q$  increases sharply. And the extreme value of energy  $E$  decreases as the parameter  $\beta$  increases. From figures (c) and (d) of Figure 7, it can be obtained that the rational number  $q$  decreases as the orbital angular momentum  $L$  increases, and there is a sharp decrease in the rational number  $q$  at the extreme value of the orbital angular momentum. Moreover, the extreme value of the orbital angular momentum  $L$  decreases as the parameter  $\beta$  increases.

In addition, we numerically calculated the energy values and orbital angular momentum values corresponding to different periodic orbits  $(z, w, v)$  when fixing the orbital angular momentum  $L$  or energy  $E$  and the parameter  $\beta$  in Tables I and II. It is obvious from Tables I and II that for the same periodic orbit, as the parameter  $\beta$  increases, both the energy and orbital angular momentum show a decreasing trend. This indicates that the energy and orbital angular momentum of the periodic orbit of the regular hairy black hole are lower than those of the periodic orbit of the Schwarzschild black hole.

Next, with the relevant parameters fixed, we have drawn the periodic trajectory diagrams with different pe-

formula.

$$q = \frac{\Delta\phi}{2\pi} - 1 = w + \frac{v}{z}, \quad (18)$$

among them,  $\Delta\phi$  is the accumulated azimuth angle between consecutive apoapsis in a periodic orbit,  $z$  is the number of leaves of the orbit,  $w$  is the number of rotations around the center, and  $v$  is the number of leaves skipped by the orbit when reaching the apex. Here

$$\Delta\phi = \oint d\phi = 2 \int_{r_1}^{r_2} \frac{d\phi}{dr} dr. \quad (19)$$

Combining equations (11) and (12), equation (18) will be rewritten as

riodic orbits  $(z, w, v)$  in Figures 8 and 9. In Figure 8, with the orbital angular momentum  $L = 0.5(L_{MBO} + L_{ISCO})$  fixed, the periodic trajectories of different rational numbers  $q$  for the Schwarzschild black hole with  $\beta = 0$  are drawn respectively, as shown by the red solid line in Figure 8; the periodic trajectory of the regular hairy black hole with  $\beta = 0.35$  is shown by the blue solid line in Figure 8. In Figure 9, with the energy  $E = 0.97$  fixed, the periodic trajectories of the Schwarzschild black hole (red solid line) and the periodic trajectory of the regular hairy black hole with  $\beta = 0.35$  (blue solid line) are also drawn. Combining Figures 8 and 9, it is clearly found that as  $z$  and  $w$  increase, the number of leaves of the periodic trajectory and the linear density number of rotations around the center increase, that is, the trajectory appears more complex.

In addition, for the same periodic orbit, compared with the Schwarzschild black hole, the periapsis radius of the test particle around the regular hairy black hole is closer to the black hole, while the apoapsis radius is farther away from the black hole. This phenomenon indicates that the introduction of the hairy parameter  $\beta$  changes the spacetime structure of the black hole, thus affecting the orbital dynamics of the particle, enabling the test particle to approach the black hole with lower energy or angular momentum and still remain on a stable periodic orbit. This change in orbital characteristics not only reveals the difference in physical essence between the regular hairy black hole and the Schwarzschild black hole, but also provides an important opportunity for testing the no-hair theorem. Through in-depth study of these orbital behaviors, we can better understand the gravitational wave radiation characteristics of the regular hairy black hole, especially the subtle differences in gravitational wave signals related to EMRI systems. Such re-

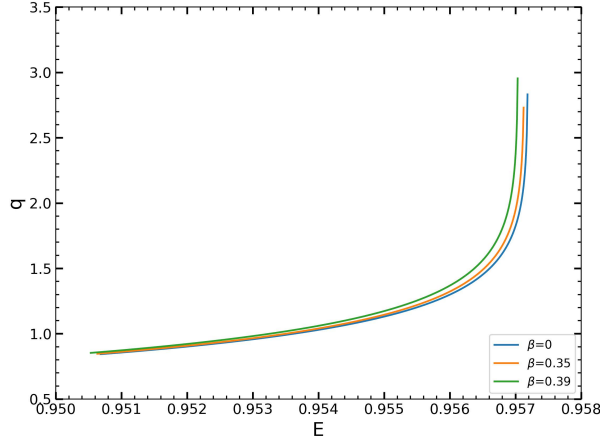
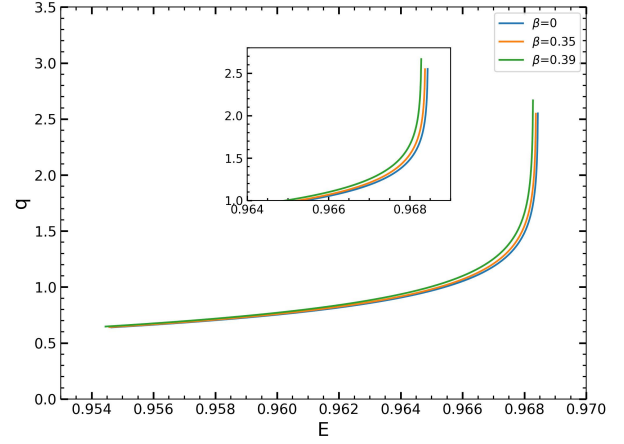
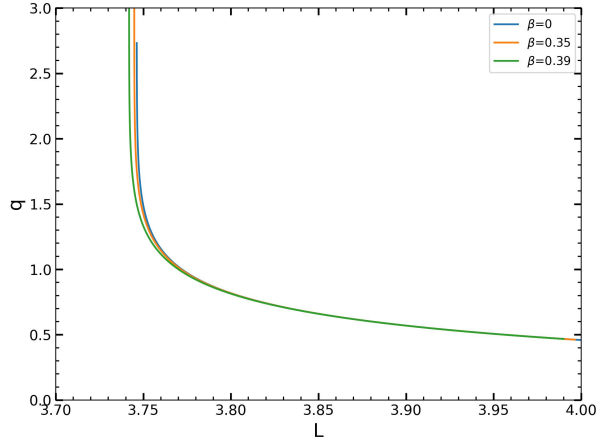
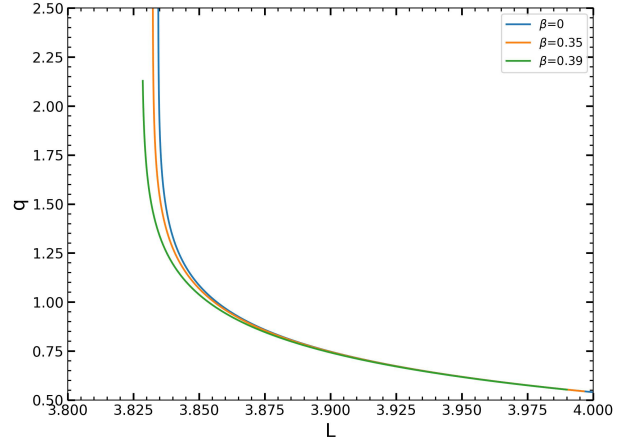
(a)  $L = 0.3L_{MBO} + 0.7L_{ISCO}$ (b)  $L = \frac{1}{2}(L_{MBO} + L_{ISCO})$ (c)  $E = 0.97$ (d)  $E = 0.98$ 

FIG. 7: Figures (a) and (b) are the relationship diagrams of the rational number  $q$  and energy  $E$  corresponding to different orbital angular momenta  $L$  and different hairy parameters  $\beta$ ; Figures (c) and (d) are the relationship diagrams of the rational number  $q$  and orbital angular momentum  $L$  corresponding to different energies  $E$  and different hairy parameters  $\beta$ . Among them,  $M = 1$ ,  $\beta = 0, 0.35, 0.39$ .

$L$	$\beta$	$E_{(1,1,0)}$	$E_{(1,2,0)}$	$E_{(2,1,1)}$	$E_{(2,2,1)}$	$E_{(3,1,2)}$	$E_{(3,2,2)}$	$E_{(4,1,3)}$	$E_{(4,2,3)}$
$0.3L_{MBO} + 0.7L_{ISCO}$	0	0.95362822	0.95708623	0.95660722	0.95717015	0.95686429	0.95717549	0.95694584	0.95718075
	0.35	0.95350389	0.95702204	0.95652338	0.95711202	0.95678934	0.95712081	0.95687439	0.95712368
	0.39	0.95326229	0.95691210	0.95637458	0.95701362	0.95665853	0.95702391	0.95675041	0.95702732
$0.5(L_{MBO} + L_{ISCO})$	0	0.96542534	0.96838291	0.96802649	0.96843431	0.96822485	0.96843848	0.96828496	0.96843977
	0.35	0.96525130	0.96831201	0.96792931	0.96836995	0.96814048	0.96837483	0.96820548	0.96837635
	0.39	0.96494576	0.96820269	0.96777272	0.96827210	0.96800689	0.96827825	0.96807995	0.96828200

TABLE I: Energy values corresponding to different periodic orbits  $(z, w, v)$ . Here, take  $L = 0.3L_{MBO} + 0.7L_{ISCO}$ ,  $L = 0.5(L_{MBO} + L_{ISCO})$  and  $M = 1$ , and the parameter  $\beta = 0, 0.35, 0.39$ .

$E$	$\beta$	$L_{(1,1,0)}$	$L_{(1,2,0)}$	$L_{(2,1,1)}$	$L_{(2,2,1)}$	$L_{(3,1,2)}$	$L_{(3,2,2)}$	$L_{(4,1,3)}$	$L_{(4,2,3)}$
0.97	0	3.77197612	3.74673495	3.74981831	3.74629399	3.74810031	3.74625875	3.74757974	3.74624803
	0.35	3.77144205	3.74538012	3.74868056	3.74488566	3.74685797	3.74484460	3.74629938	3.74483195
	0.39	3.77010706	3.74254238	3.74621973	3.74195436	3.74421508	3.74190288	3.74359045	3.74188674
0.98	0	3.85671457	3.83477572	3.83720996	3.83446575	3.83582295	3.83444322	3.83541529	3.83443659
	0.35	3.85573037	3.83275139	3.83542644	3.83238990	3.83391929	3.83236232	3.83346947	3.83235406
	0.39	3.85351356	3.82875540	3.83183053	3.82830572	3.83012430	3.82826912	3.82960461	3.82825792

TABLE II: Orbital angular momentum values corresponding to different periodic orbits  $(z, w, v)$ . Here, take  $E = 0.97$ ,  $E = 0.98$  and  $M = 1$ , and the parameter  $\beta = 0, 0.35, 0.39$ .

search provides a theoretical basis for distinguishing different types of black holes through gravitational wave observations in the future, helps to further deepen our understanding of black hole structure and its dynamics, and provides a new perspective for the research of gravitational wave astronomy.

In general, we have studied the relevant properties of MBO, ISCO and periodic orbits. These studies will contribute to the understanding of periodic orbits and help analyze the long-term behavior of complex systems. For example, there are usually multiple unstable periodic orbits in chaotic systems. Studying these orbits can provide a new perspective for revealing the fundamental mechanism and dynamic structure of the system. In addition, in the EMRI system, periodic orbits can radiate gravitational waves[35, 38]. This prompts us to conduct a preliminary exploration of the periodic orbits of a timelike test particle around the regular hairy black hole and the gravitational waves radiated by the EMRI system. This will be shown in the next section.

#### IV. GRAVITATIONAL WAVE RADIATION OF PERIODIC ORBITS

This section will study the gravitational waves radiated by the periodic orbits of the particle around a regular hairy black hole. First of all, in a binary star system, here we consider the EMRI system. The periodic motion of the timelike test particle will radiate gravitational waves, which in turn leads to a decrease in orbital angular momentum and energy, making the particle's orbit slowly decay and approach the black hole, and eventually it will be merged by the black hole. Due to the slow nature of the above process, it can take several years in the gravitational wave frequency band, and the decrease in orbital angular momentum and energy is very small compared to the total energy of the system. Therefore, for a single periodic orbit, the adiabatic approximation can be applied for study[74, 75]. In addition, to quickly and effectively obtain the gravitational waveforms of the periodic orbits of the particle, we use the Kludge waveform method[76].

The generation of Kludge waveforms is divided into

two stages: (1) calculation of the trajectory (the periodic orbits from the previous section); (2) calculation of the gravitational waveforms from any trajectory. For the second stage, the gravitational waveforms due to orbital radiation can be calculated using the following formula based on the quadrupole moment formula of gravitational radiation. To ensure consistency in the unit system, we will retain the use of  $G$  and  $c$ . The quadrupole moment formula is

$$h_{ij} = \frac{4G\eta M}{c^4 D_L} (v_i v_j - \frac{Gm}{r} n_i n_j), \quad (21)$$

here,  $M$  is the mass of the black hole,  $m$  is the mass of the test particle,  $v$  is the relative velocity,  $\mathbf{n}$  is the direction of the separation vector of the EMRI system,  $\eta = \frac{Mm}{(M+m)^2}$  is the symmetric mass ratio, and  $D_L$  is the luminosity distance from the EMRI system to the detector. To construct the gravitational wave waveform, we introduce a detector adaptive coordinate system  $(X, Y, Z)$  outside the original coordinate system  $(x, y, z)$ [77], and its coordinate directions are

$$\begin{aligned} \mathbf{e}_X &= (\cos \zeta, -\sin \zeta, 0), \\ \mathbf{e}_Y &= (\cos \iota \sin \zeta, \cos \iota \cos \zeta, -\sin \iota), \\ \mathbf{e}_Z &= (\sin \iota \sin \zeta, \sin \iota \cos \zeta, \cos \iota). \end{aligned} \quad (22)$$

Here, using  $\mathbf{e}_X$  and  $\mathbf{e}_Y$  as vector bases, there exists

$$\begin{aligned} h_+ &= \frac{1}{2} (e_X^i e_X^j - e_Y^i e_Y^j) h_{ij}, \\ h_\times &= \frac{1}{2} (e_X^i e_Y^j + e_Y^i e_X^j) h_{ij}. \end{aligned} \quad (23)$$

According to equations (21)-(23), the corresponding gravitational wave is obtained[77].

$$h_+ = -\frac{2\eta}{c^4 D_L} \frac{(GM)^2}{r} (1 + \cos^2 \iota) \cos(2\phi + 2\zeta), \quad (24)$$

$$h_\times = -\frac{4\eta}{c^4 D_L} \frac{(GM)^2}{r} \cos \iota \sin(2\phi + 2\zeta). \quad (25)$$

Among them,  $\iota$  is the inclination angle between the orbital plane of the test particle and the  $X - Y$  plane in the

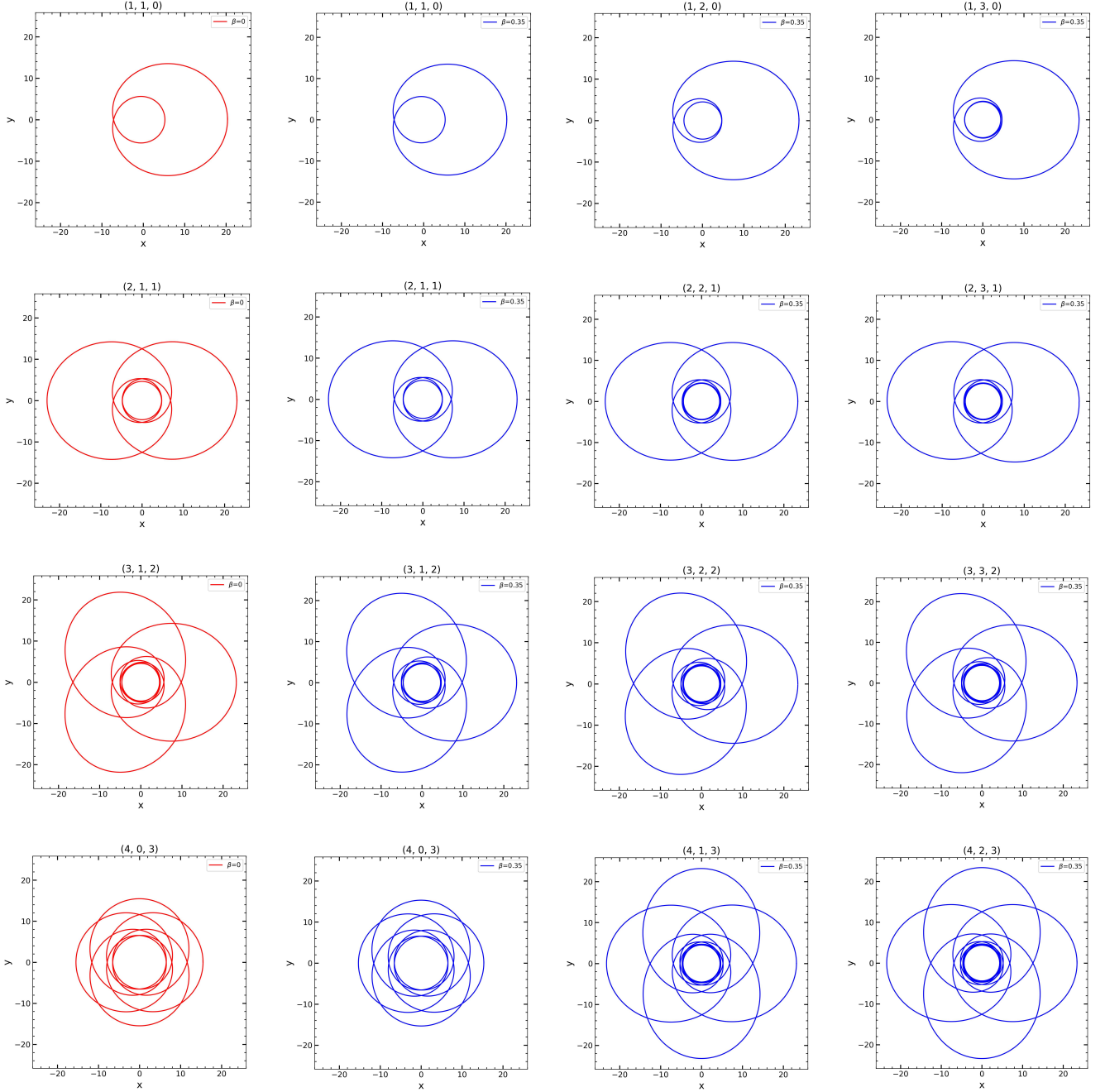


FIG. 8: Periodic trajectory diagrams of different periodic orbits  $(z, w, v)$ . Among them, the red solid line is the periodic trajectory of the Schwarzschild black hole; the blue solid line is the periodic trajectory of the regular hairy black hole with parameter  $\beta = 0.35$ . Here, the orbital angular momentum  $L = 0.5(L_{MBO} + L_{ISCO})$  and  $M = 1$  are fixed.

detector coordinate system,  $\zeta$  is the latitude angle and  $\phi$  is the phase angle.

To plot the corresponding gravitational waveforms, we consider the gravitational waves radiated from a complete periodic orbit and set the parameters of the EMRI system as  $\iota = \frac{\pi}{4}$ ,  $\zeta = \frac{\pi}{4}$ ,  $M = 10^7 M_\odot$ , and  $m = 10 M_\odot$ , where  $M_\odot$  is the solar mass. The luminosity distance is

$D_L = 200 \text{ Mpc}$ . Next, in figures 10 and 11, we consider two classical periodic orbits: (3,2,2) and (4,2,3).

According to figures 10 and 11, the gravitational waves exhibit notable zoom-whirl behavior over a complete period. Combining this with the trajectory periodic diagram on the left, it can be observed that during the scaling phase, when the orbit is highly elliptical, the gravi-

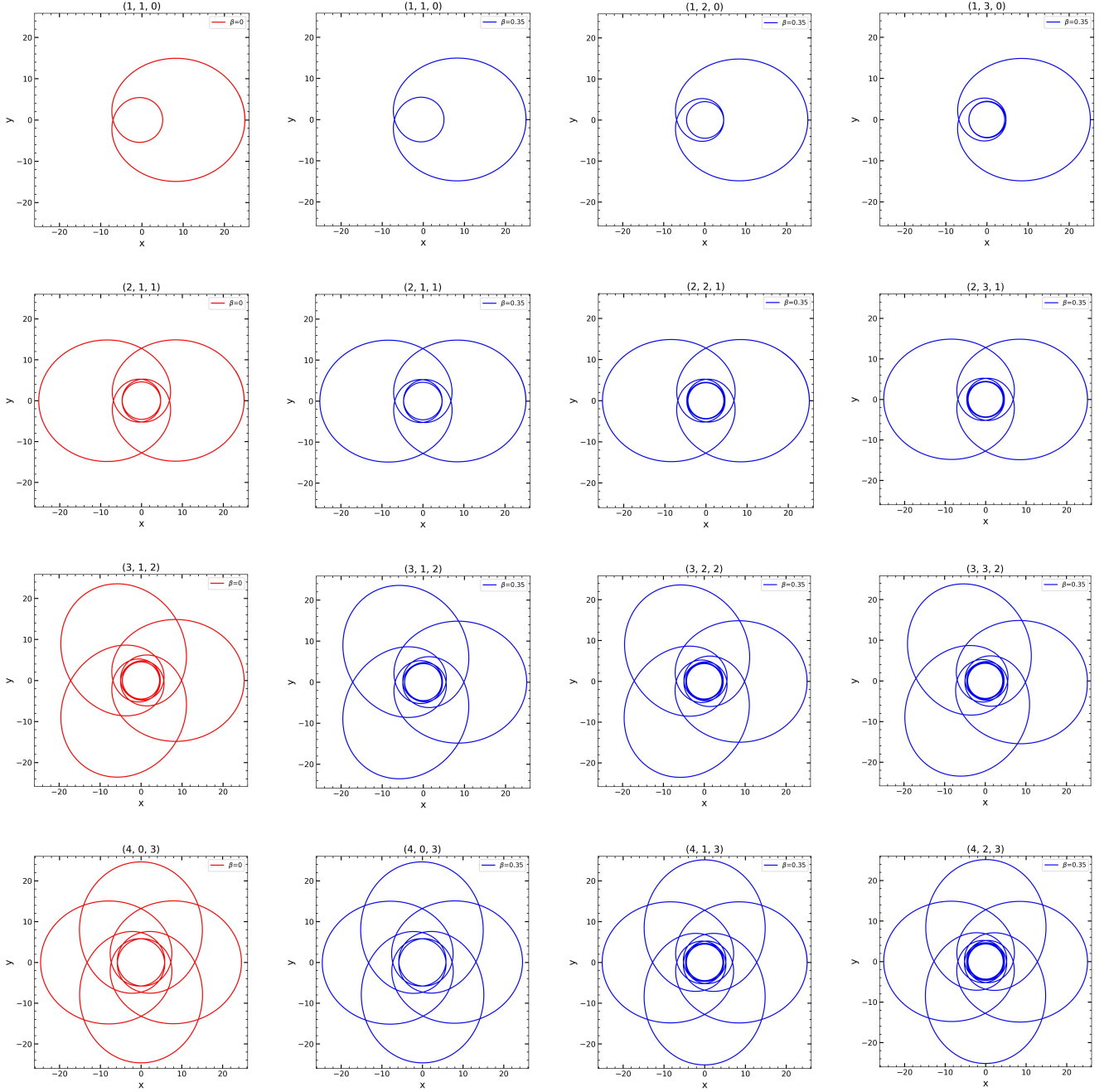


FIG. 9: Periodic trajectory diagrams of different periodic orbits  $(z, w, v)$ . Among them, the red solid line is the periodic trajectory of the Schwarzschild black hole; the blue solid line is the periodic trajectory of the regular hairy black hole with parameter  $\beta = 0.35$ . Here, the energy  $E = 0.97$  and  $M = 1$  are fixed.

tational wave waveform changes relatively smoothly. In contrast, during the rotation phase when the orbit approaches circularity, the gravitational wave waveform undergoes significant changes. These variations in the gravitational waveforms correspond to the precession of the orbit (the number of orbital leaves), indicating that the gravitational wave signals reflect the periodic characteristics of the system's orbit.

In addition, compared with the Schwarzschild black hole ( $\beta = 0$ ), the existence of the hairy parameter  $\beta$  has made subtle corrections to the gravitational wave waveform. Specifically, it is manifested as an increase in the amplitude of the gravitational wave, a change in the period, and a change in the phase. Although for a single periodic orbit, these differences are not significant. But throughout the zoom-whirl stage, the test particle contin-

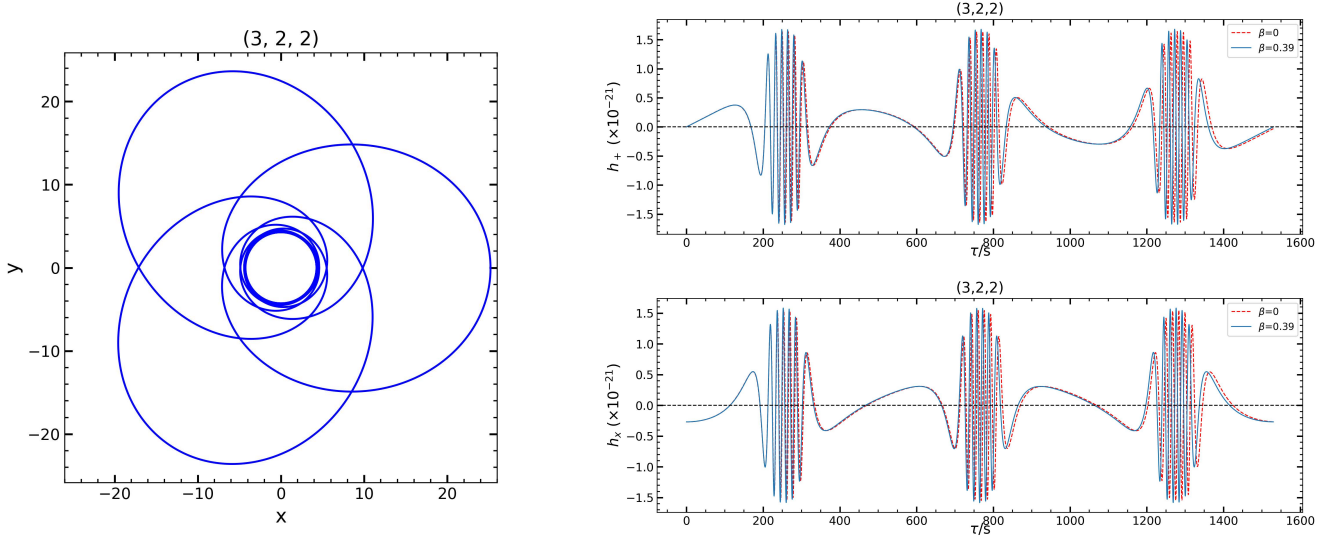


FIG. 10: The left side shows the trajectory of the periodic orbit  $(z, w, v) = (3, 2, 2)$ . The right side features a red dashed line representing the gravitational wave of a Schwarzschild black hole, with parameters set to  $\beta = 0$  and  $q = 2 + \frac{2}{3}$ . The light blue solid line represents the gravitational wave of a regular hairy black hole, with parameters set to  $\beta = 0.39$  and  $q = 2 + \frac{2}{3}$ .

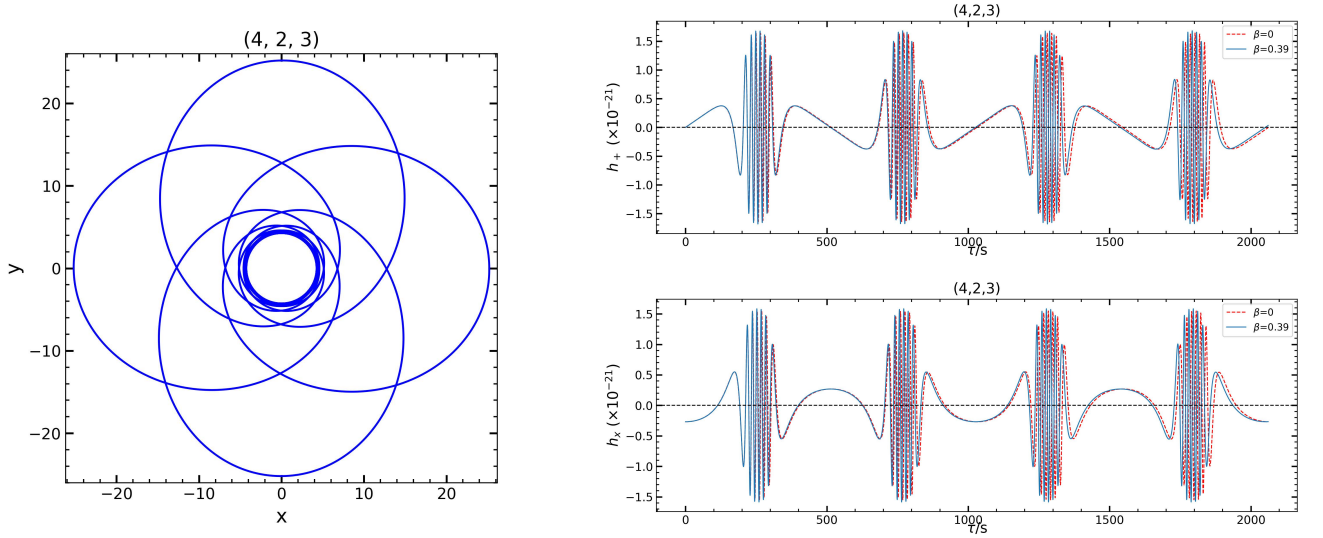


FIG. 11: The left side shows the trajectory of the periodic orbit  $(z, w, v) = (4, 2, 3)$ . The right side features a red dashed line representing the gravitational wave of a Schwarzschild black hole, with parameters set to  $\beta = 0$  and  $q = 2 + \frac{2}{3}$ . The light blue solid line represents the gravitational wave of a regular hairy black hole, with parameters set to  $\beta = 0.39$  and  $q = 2 + \frac{2}{3}$ .

ously radiates gravitational waves, causing the orbital angular momentum  $L$  and energy  $E$  of the system to continuously dissipate, and the particle gradually migrates to a periodic orbit closer to the black hole. As the orbit evolves, the phase shift, amplitude change, and cumulative effect of the period of gravitational waves continue to increase, resulting in a significant shift in the waveform during long-term evolution. This shift not only provides

potential favorable conditions for accurate gravitational wave detection, but also reveals the influence of hairy parameters on the dynamics of matter near black holes, and then provides a unique observation window for exploring the hairy structure of black holes. Through accurate modeling and analysis of these cumulative effects, we are expected to be more sensitively able to capture the differences between the regular hairy black hole and the

Schwarzschild black hole, thus providing strong evidence for testing the no-hair theorem and the subtle features of the black hole gravitational field.

It is worth noting that in the research based on the EMRI system, the waveform of the gravitational wave radiation of the periodic orbit we obtained is not an exact solution. This is because in the calculation we adopt the adiabatic approximation condition and use the quadrupole moment formula (formula (21)), ignoring the multipole moment contributions above the second order. However, in spite of this, our calculation results can still reflect the basic characteristics of the gravitational wave radiation of periodic orbits. Current research shows that analyzing the periodic orbit evolution in the EMRI system has important physical significance[78]. In addition, the EMRI system is considered as one of the key signal sources in gravitational wave observations[25, 29]. The study of this system not only helps to deeply understand the nature of black holes[25] but also can help explore whether there is dark matter around black holes[32] and impose more precise constraints on cosmological parameters[33]. In conclusion, the EMRI system has extremely high research value in gravitational wave astronomy.

## V. SUMMARY AND DISCUSSION

In this paper, we study the geodesic motion of a time-like particle around the regular hairy black hole. First, the effective potential of the particle's radial motion is calculated, and the relationship between the relevant parameters of MBO and ISCO ( $r_{ISCO}$ ,  $L_{ISCO}$ , and  $E_{ISCO}$ ) and the hairy parameter  $\beta$  is further analyzed. The results show that in the initial stage, with the change of the hairy parameter  $\beta$ , the relevant parameters of MBO and ISCO do not change significantly, which indicates that at this time it is difficult to distinguish the regular hairy black hole from the Schwarzschild black hole. However, as the hairy parameter  $\beta$  further increases,  $r_{MBO}$ ,  $L_{MBO}$ ,  $r_{ISCO}$ ,  $L_{ISCO}$ , and  $E_{ISCO}$  all decrease significantly. Then, through the analysis of orbital angular momentum  $L$  and energy  $E$ , we find that there is an allowed parameter space, and as the hairy parameter  $\beta$  increases, the allowed region gradually expands and moves towards lower angular momentum and higher energy.

In addition, we further explore the periodic orbital behavior of the regular hairy black hole. Research shows that the rational number parameter  $q$  of the periodic orbit increases with the increase of orbital energy and decreases with the increase of orbital angular momentum. Further analysis shows that as the hairy parameter  $\beta$  increases, the extreme values of orbital angular momentum and energy both show a downward trend. In addition, through numerical analysis of different periodic orbits ( $z, w, v$ ), we come to the conclusion that for the same periodic orbit, a regular hairy black hole has lower angular momentum  $L$  and energy  $E$  than a Schwarzschild

black hole. Further analysis from the periodic trajectory shows that the test particle around a regular hairy black hole can remain stable on a periodic orbit closer to the black hole. It is speculated that this phenomenon may be related to the fact that the hairy parameter  $\beta$  changes the spacetime structure of the black hole. Therefore, the difference in periodic orbits between the Schwarzschild black hole and the regular hairy black hole not only provides a new perspective for testing the no-hair theorem but also gives us the opportunity to further understand the influence of hairy parameters on black holes and the spacetime structure characteristics of the regular hairy black hole through these differences.

Next, we conduct a preliminary study on the characteristics of gravitational waves radiated by periodic orbits in the EMRI system under the background of the regular hairy black hole. Through analysis, we find that within a complete orbital period, the gravitational wave signal presents a significant zoom-whirl behavior. Its variation characteristics correspond to the periodic orbit and reflect the characteristics of periodic orbit dynamics. In addition, the research results show that the hairy parameter  $\beta$  introduces minor corrections to the phase, amplitude, and period of the gravitational wave waveform. As the orbit continues to evolve, the phase shift, amplitude change, and cumulative effect of the period of gravitational waves continue to increase, resulting in a significant shift in the waveform during long-term evolution. This is conducive to distinguishing the Schwarzschild black hole from the hairy black hole and testing the no-hair theorem. Moreover, this phenomenon provides a potential advantage for high-precision measurement in gravitational wave detection.

It is worth noting that in this work, we consider the motion within one period, which is sufficient for our analysis. However, in the case of long periods, it is necessary for us to consider the reaction of gravitational radiation on the orbit. And in the real cosmic environment, black holes are usually rotating and their surrounding environment is full of matter, which makes it particularly important to consider the influence of environmental factors on the orbit. In addition, the gravitational wave signal radiated by the EMRI system is relatively weak and requires a long time of accumulation to obtain a sufficient signal-to-noise ratio. Therefore, the design of waveform templates not only needs to have high precision but also high efficiency. These issues are key challenges that need to be urgently addressed in future research.

## ACKNOWLEDGEMENTS

We acknowledge the anonymous referee for a constructive report that has significantly improved this paper. This work was supported by Guizhou Provincial Basic Research Program (Natural Science) (Grant No. QianKeHeJiChu-[2024]Young166), the Special Natural Science Fund of Guizhou University (Grant

No.X2022133), the National Natural Science Foundation of China (Grant No. 12365008) and the Guizhou Provin-

cial Basic Research Program (Natural Science) (Grant No. QianKeHeJiChu-ZK[2024]YiBan027).

- 
- [1] K. Akiyama *et al.* (Event Horizon Telescope), *Astrophys. J. Lett.* **875**, L1 (2019), arXiv:1906.11238 [astro-ph.GA].
- [2] K. Akiyama *et al.* (Event Horizon Telescope), *Astrophys. J. Lett.* **875**, L4 (2019), arXiv:1906.11241 [astro-ph.GA].
- [3] K. Akiyama *et al.* (Event Horizon Telescope), *Astrophys. J. Lett.* **875**, L5 (2019), arXiv:1906.11242 [astro-ph.GA].
- [4] K. Akiyama *et al.* (Event Horizon Telescope), *Astrophys. J. Lett.* **875**, L6 (2019), arXiv:1906.11243 [astro-ph.GA].
- [5] J. R. Oppenheimer and H. Snyder, *Phys. Rev.* **56**, 455 (1939).
- [6] V. P. Frolov and I. D. Novikov, “Spherically symmetric black holes,” in *Black Hole Physics: Basic Concepts and New Developments* (Springer Netherlands, Dordrecht, 1998) pp. 12–55.
- [7] R. M. Wald, *General Relativity* (Chicago Univ. Pr., Chicago, USA, 1984).
- [8] C. W. Misner, K. S. Thorne, J. A. Wheeler, and D. I. Kaiser, *Gravitation* (2018).
- [9] R. P. Kerr, *Phys. Rev. Lett.* **11**, 237 (1963).
- [10] H. Reissner, *Annalen Phys.* **355**, 106 (1916).
- [11] J. C. Graves and D. R. Brill, *Phys. Rev.* **120**, 1507 (1960).
- [12] G. Nordström, *Koninklijke Nederlandse Akademie van Wetenschappen Proceedings Series B Physical Sciences* **20**, 1238 (1918).
- [13] E. T. Newman, R. Couch, K. Chinnapared, A. Exton, A. Prakash, and R. Torrence, *J. Math. Phys.* **6**, 918 (1965).
- [14] B. Carter, *Phys. Rev.* **174**, 1559 (1968).
- [15] J. D. Bekenstein, *Phys. Rev. D* **5**, 1239 (1972).
- [16] R. Ruffini and J. A. Wheeler, *Phys. Today* **24**, 30 (1971).
- [17] J. D. Bekenstein, *Annals Phys.* **82**, 535 (1974).
- [18] B. C. Xanthopoulos and T. E. Dialynas, *J. Math. Phys.* **33**, 1463 (1992).
- [19] P. Bizon, *Phys. Rev. Lett.* **64**, 2844 (1990).
- [20] E. Contreras, J. Ovalle, and R. Casadio, *Phys. Rev. D* **103**, 044020 (2021), arXiv:2101.08569 [gr-qc].
- [21] H. Elvang, R. Emparan, D. Mateos, and H. S. Reall, *Phys. Rev. Lett.* **93**, 211302 (2004), arXiv:hep-th/0407065.
- [22] R. Emparan and H. S. Reall, *Phys. Rev. Lett.* **88**, 101101 (2002), arXiv:hep-th/0110260.
- [23] J. Ovalle, R. Casadio, and A. Giusti, *Phys. Lett. B* **844**, 138085 (2023), arXiv:2304.03263 [gr-qc].
- [24] S. W. Hawking, *Phys. Rev. D* **13**, 191 (1976).
- [25] P. Amaro-Seoane, J. R. Gair, M. Freitag, M. Coleman Miller, I. Mandel, C. J. Cutler, and S. Babak, *Class. Quant. Grav.* **24**, R113 (2007), arXiv:astro-ph/0703495.
- [26] K. Glampedakis, *Class. Quant. Grav.* **22**, S605 (2005), arXiv:gr-qc/0509024.
- [27] B. P. Abbott *et al.* (LIGO Scientific, Virgo), *Phys. Rev. Lett.* **116**, 061102 (2016), arXiv:1602.03837 [gr-qc].
- [28] B. P. Abbott *et al.* (LIGO Scientific, Virgo), *Phys. Rev. Lett.* **116**, 241102 (2016), arXiv:1602.03840 [gr-qc].
- [29] S. Babak, J. Gair, A. Sesana, E. Barausse, C. F. Sopuerta, C. P. L. Berry, E. Berti, P. Amaro-Seoane, A. Petiteau, and A. Klein, *Phys. Rev. D* **95**, 103012 (2017), arXiv:1703.09722 [gr-qc].
- [30] X.-J. Yue, W.-B. Han, and X. Chen, *Astrophys. J.* **874**, 34 (2019), arXiv:1802.03739 [gr-qc].
- [31] X.-J. Yue and W.-B. Han, *Phys. Rev. D* **97**, 064003 (2018), arXiv:1711.09706 [gr-qc].
- [32] O. A. Hannuksela, K. C. Y. Ng, and T. G. F. Li, *Phys. Rev. D* **102**, 103022 (2020), arXiv:1906.11845 [astro-ph.CO].
- [33] B. F. Schutz, *Nature* **323**, 310 (1986).
- [34] P. Amaro-Seoane, *Phys. Rev. D* **99**, 123025 (2019), arXiv:1903.10871 [astro-ph.GA].
- [35] J. Levin and G. Perez-Giz, *Phys. Rev. D* **77**, 103005 (2008), arXiv:0802.0459 [gr-qc].
- [36] R. Grossman and J. Levin, *Phys. Rev. D* **79**, 043017 (2009), arXiv:0811.3798 [gr-qc].
- [37] J. Levin and B. Grossman, *Phys. Rev. D* **79**, 043016 (2009), arXiv:0809.3838 [gr-qc].
- [38] K. Glampedakis and D. Kennefick, *Phys. Rev. D* **66**, 044002 (2002), arXiv:gr-qc/0203086.
- [39] C. M. Will, *Theory and Experiment in Gravitational Physics* (1993).
- [40] L. Iorio, *Phys. Rev. D* **84**, 124001 (2011), [Erratum: *Phys. Rev. D* **106**, 129902 (2022)], arXiv:1107.2916 [gr-qc].
- [41] A. Amorim *et al.* (GRAVITY), *Mon. Not. Roy. Astron. Soc.* **489**, 4606 (2019), arXiv:1908.06681 [astro-ph.GA].
- [42] A. Hees *et al.*, *Phys. Rev. Lett.* **118**, 211101 (2017), arXiv:1705.07902 [astro-ph.GA].
- [43] R. Della Monica and I. de Martino, *Phys. Rev. D* **108**, L101303 (2023), arXiv:2305.10242 [gr-qc].
- [44] M. Grould, F. H. Vincent, T. Paumard, and G. Perrin, *Astron. Astrophys.* **608**, A60 (2017), arXiv:1709.04492 [astro-ph.HE].
- [45] M. De Laurentis, I. De Martino, and R. Lazkoz, *Phys. Rev. D* **97**, 104068 (2018), arXiv:1801.08136 [gr-qc].
- [46] J. Levin and G. Perez-Giz, *Phys. Rev. D* **79**, 124013 (2009), arXiv:0811.3814 [gr-qc].
- [47] G. Perez-Giz and J. Levin, *Phys. Rev. D* **79**, 124014 (2009), arXiv:0811.3815 [gr-qc].
- [48] R. Grossman, J. Levin, and G. Perez-Giz, *Phys. Rev. D* **85**, 023012 (2012), arXiv:1105.5811 [gr-qc].
- [49] Y.-K. Lim and Z. C. Yeo, *Phys. Rev. D* **109**, 024037 (2024), arXiv:2401.13894 [gr-qc].
- [50] H.-Y. Lin and X.-M. Deng, *Phys. Dark Univ.* **31**, 100745 (2021).
- [51] J. Healy, J. Levin, and D. Shoemaker, *Phys. Rev. Lett.* **103**, 131101 (2009), arXiv:0907.0671 [gr-qc].
- [52] V. Misra and J. Levin, *Phys. Rev. D* **82**, 083001 (2010), arXiv:1007.2699 [gr-qc].
- [53] G. Z. Babar, A. Z. Babar, and Y.-K. Lim, *Phys. Rev. D* **96**, 084052 (2017), arXiv:1710.09581 [gr-qc].
- [54] Z.-Y. Tu, T. Zhu, and A. Wang, *Phys. Rev. D* **108**, 024035 (2023), arXiv:2304.14160 [gr-qc].
- [55] R. Gervalle and M. S. Volkov, *Phys. Rev. Lett.* **133**, 171402 (2024), arXiv:2406.14357 [hep-th].
- [56] M. Astorino, *Phys. Rev. D* **88**, 104027 (2013), arXiv:1307.4021 [gr-qc].
- [57] H.-Y. Lin and X.-M. Deng, *Eur. Phys. J. C* **83**, 311 (2023).

- [58] L. G. Collodel, D. D. Doneva, and S. S. Yazadjiev, *Astrophys. J.* **910**, 52 (2021), arXiv:2101.05073 [astro-ph.HE].
- [59] M. Armano *et al.*, *Phys. Rev. Lett.* **116**, 231101 (2016).
- [60] W.-R. Hu and Y.-L. Wu, *Natl. Sci. Rev.* **4**, 685 (2017).
- [61] J. Luo *et al.* (TianQin), *Class. Quant. Grav.* **33**, 035010 (2016), arXiv:1512.02076 [astro-ph.IM].
- [62] U. Nucamendi and M. Salgado, *Phys. Rev. D* **68**, 044026 (2003), arXiv:gr-qc/0301062.
- [63] K. G. Zloshchastiev, *Phys. Rev. Lett.* **94**, 121101 (2005), arXiv:hep-th/0408163.
- [64] E. Winstanley and N. E. Mavromatos, *Phys. Lett. B* **352**, 242 (1995), arXiv:hep-th/9503034.
- [65] N. E. Mavromatos and E. Winstanley, *J. Math. Phys.* **39**, 4849 (1998), arXiv:gr-qc/9712049.
- [66] I. Bena and P. Kraus, *Phys. Rev. D* **72**, 025007 (2005), arXiv:hep-th/0503053.
- [67] V. Jejjala, O. Madden, S. F. Ross, and G. Titchener, *Phys. Rev. D* **71**, 124030 (2005), arXiv:hep-th/0504181.
- [68] J. Ovalle, R. Casadio, E. Contreras, and A. Sotomayor, *Phys. Dark Univ.* **31**, 100744 (2021), arXiv:2006.06735 [gr-qc].
- [69] J. Ovalle, R. Casadio, R. d. Rocha, A. Sotomayor, and Z. Stuchlik, *Eur. Phys. J. C* **78**, 960 (2018), arXiv:1804.03468 [gr-qc].
- [70] R. Avalos, P. Bargueño, and E. Contreras, *Fortsch. Phys.* **71**, 2200171 (2023), arXiv:2303.04119 [gr-qc].
- [71] B. Gao and X.-M. Deng, *Annals Phys.* **418**, 168194 (2020).
- [72] D. Pugliese, H. Quevedo, and R. Ruffini, *Phys. Rev. D* **83**, 104052 (2011), arXiv:1103.1807 [gr-qc].
- [73] C. W. Misner, K. S. Thorne, J. A. Wheeler, and D. I. Kaiser, *Gravitation* (2018).
- [74] S. A. Hughes, S. Drasco, E. E. Flanagan, and J. Franklin, *Phys. Rev. Lett.* **94**, 221101 (2005), arXiv:gr-qc/0504015.
- [75] P. A. Sundararajan, G. Khanna, and S. A. Hughes, *Phys. Rev. D* **76**, 104005 (2007), arXiv:gr-qc/0703028.
- [76] S. Babak, H. Fang, J. R. Gair, K. Glampedakis, and S. A. Hughes, *Phys. Rev. D* **75**, 024005 (2007), [Erratum: *Phys.Rev.D* 77, 04990 (2008)], arXiv:gr-qc/0607007.
- [77] C. M. Will, “Gravity: Newtonian, Post-Newtonian, and General Relativistic,” in *Gravity: Where Do We Stand?*, edited by R. Peron, M. Colpi, V. Gorini, and U. Moschella (2016) pp. 9–72.
- [78] Y. Mino, M. Sasaki, and T. Tanaka, *Phys. Rev. D* **55**, 3457 (1997), arXiv:gr-qc/9606018.